

SURROGATE-BASED MODELING AND MULTI-OBJECTIVE OPTIMIZATION TECHNIQUES FOR THERMO-FLUID & ENERGY SYSTEMS

Young-Chang Cho
University of Michigan
Ann Arbor, MI, USA

Wenbo Du
University of Michigan
Ann Arbor, MI, USA

Amit Gupta
University of Michigan
Ann Arbor, MI, USA

Chien-Chou Tseng
University of Michigan
Ann Arbor, MI, USA

Ann Marie Sastry
University of Michigan
Ann Arbor, MI, USA

Wei Shyy
Hong Kong University of
Science and Technology
Clear Water Bay, Hong Kong

ABSTRACT

Successful modeling and/or design of thermo-fluid and energy systems often requires one to address the impact of multiple “design variables” on the prescribed outcome. There are often multiple, competing objectives based on which we assess the outcome of optimization. Since accurate, high fidelity models are typically time consuming and computationally expensive, comprehensive evaluations can be conducted only if an efficient framework is available. Furthermore, informed decisions of model/hardware’s overall performance rely on an adequate understanding of the global, not local, sensitivity of the individual design variables on the objectives. The surrogate-based approach, which involves approximating the objectives as continuous functions of design variables from limited data, offers a rational framework to reduce the number of important input variables, i.e., the dimension of a design or modeling space. In this paper, we discuss the fundamental issues that arise in surrogate-based analysis and optimization, highlighting concepts, methods, techniques, as well as practical implications. To aid the discussions of the issues involved, we will summarize recent efforts in investigating cryogenic cavitating flows, active flow control based on dielectric barrier discharge concepts, and Li-ion batteries.

NOMENCLATURE

\mathbf{b} Vector of polynomial coefficients
 C Cycling rate, where 1C is the rate required to charge/discharge the cell in one hour
 D Characteristic length scale [m]
 D_s Solid diffusion coefficient [m²/s]
 E Expectation value
 f_v Vapor mass fraction/Frequency of applied voltage [kHz]
 F_x x-directional Lorentzian force [mN/m]
 $F_{x,S}$ Domain averaged x-directional Lorentzian force [mN/m]

$F_{x,ST}$ Time and domain averaged x-directional Lorentzian force [mN/m]
 h Enthalpy [kJ/kg]
 L Latent heat [kJ/kg]
 m^+ Source term in cavitation model [1/s]
 m^- Sink term in cavitation model [1/s]
 n_p Particle number density of species p [1/m³]
 N_s Number of sampled design points
 N_{RBF} Number of neural basis functions
 N_v Number of design variables
 P Pressure [N/cm²]; power input due to the charge current through the upper electrode [W]
 P_v Saturation vapor pressure [N/cm²]
 P_{diff} L₂ norm between experiment and predicted pressure [N/cm²]
 P_T Time averaged power input due to the charge current through the upper electrode [W]
 Pr Prandtl number
 r_f Positive-to-negative polarity time ratio of applied voltage waveform
 R^2_{adj} Adjusted coefficient of determination
 $R_{s,p}$ Solid particle radius in positive electrode [μm]
 \mathbf{s} Vector of neuron position
 S Area of computational domain for gas [m²]
 S_M Main sensitivity index
 S_T Total sensitivity index
 t_∞ Reference time scale, $t_\infty = D/U_\infty$ [s]
 T Temperature [K]; Period of applied voltage [s]
 T_{diff} L₂ norm between experiment and predicted temperature [K]
 u Velocity [m/s]
 u_p Particle bulk velocity of species p , ($u_{x,p}$, $u_{y,p}$, $u_{z,p}$) [m/s]
 U_∞ Reference velocity [m/s]
 V Variance
 V_{app} Applied voltage to the upper electrode [kV]
 \mathbf{x} Vector of design variables; Space variable [m]
 y Objective function

\hat{y}	Surrogate approximation of objective function
\bar{y}	Mean value of objective function
Z	Systematic departure
α_l	Liquid volume fraction
β	Spread coefficient of radial basis neural network
ϵ_d	Dielectric constant of insulator
μ	Dynamic viscosity [kg/m-s]
ρ	Density [kg/m ³]
σ	Electronic conductivity [S/m]
σ_∞	Cavitation number based on the free stream temperature
σ_a	RMS error of polynomial response surface at sampled points
τ	Dimensionless time

INTRODUCTION

The notion of design variables influencing system performance can be found in numerous thermo-fluid and energy systems. In the computational modeling context, the design variables can be adjustable parameters associated with a given mathematical model under different operating conditions and scaling parameters. In the hardware design context, they are often geometry, materials, and operating variables. In both situations, there are often multiple, competing objectives based on which we assess the outcome of optimization. Since accurate, high fidelity models are typically time consuming and computationally expensive, comprehensive evaluations can be conducted only if an efficient framework is available. Furthermore, informed decisions concerning a model or hardware system's overall performance rely on an adequate understanding of the global, not local, sensitivity of the individual design variables on the objectives.

In reality, most engineering system and modeling designs are conducted as open loop, feed-forward processes. For example, for turbine design in aerospace and mechanical engineering, one design iteration for a given set of engine balance conditions may currently take up to several weeks, with just the blade geometry design sub-iteration phases taking several days each. The quest for an acceptable blade surface velocity distribution is accomplished with many ad hoc rules in what is essentially a manual trial-and-error process. A systematic approach capable of identifying design optimality and comparing possible trade-offs can significantly improve the productivity and shorten the design cycle.

Objective and efficient evaluation of advanced designs can be facilitated by development and implementation of systematic optimization and sensitivity evaluation methods. To date, the majority of the effort in design optimization has relied on gradient-based search algorithms. These methods work iteratively through a sequence of local sub-problems, which approximate objective and constraint functions for a sub-region of the design space, e.g., by linearization using computed sensitivities. Major challenges for these optimization approaches are the robust and speedy computation of sensitivity coefficients.

Yet despite recent research advances, formal design optimization has yet to see practical use in real design scenarios. The reasons are several-fold:

- (i) The objective functions are likely to be multi-modal or discontinuous over the broad design space [1], rendering gradient search methods insufficient by themselves. Additionally, the usual practice to combine multiple goals into a single quantitative objective function is too restrictive. Qualitative goals are often required to correctly characterize a problem (e.g., maximizing a turbine blade's aerodynamic efficiency with a smooth, monotonic surface velocity distribution, while spreading heat load as uniformly as possible). These goals may have arisen from diverse disciplines and are usually treated sequentially by different groups.
- (ii) It is inadequate to think of the final product of a design process as a mere geometry. A "design" really encompasses a whole set of operating, manufacturing, and project level decisions.
- (iii) As the interaction between numerical simulation and physical test data becomes stronger, the future engineering knowledge base is likely to consist of various heterogeneous data sources including experimental data, past product experiences, semi-empirical modeling, and high fidelity simulations. Some data are anecdotal; others cover only small "patches" of the physical domain but are still useful for "reality checks". A unified framework needs to be constructed for representation, capturing and mining of all these data types so the response functions can be continuously improved.

The surrogate-based approach is an excellent technique for analysis and probing of such issues. It also offers a rational framework to reduce the number of important input variables, i.e., the dimension of a design or modeling space. The surrogates can be constructed using data drawn from pre-computed high-fidelity simulations and physical measurements, and provide fast evaluations of the various modeling and design scenarios, thereby making sensitivity and optimization studies feasible. As discussed by Shyy et al. [2], they have several advantages when compared to local gradient-based methods:

- (i) They do not require calculation of the local sensitivity of each design variable,
- (ii) They can utilize the information collected from various sources and by different tools,
- (iii) They offer multi-criterion optimization,
- (iv) They can handle the existence of multiple design points and trade-offs,
- (v) They easily perform tasks in parallel, and
- (vi) They can often effectively filter the noise intrinsic to numerical and experimental data.

However, there are uncertainties in predictions using this approach, such as empiricism in computational models and surrogate model errors. We have developed methods to estimate and to reduce such uncertainties using multiple criteria because a single criterion may underestimate the error. We have advanced the techniques of using an ensemble of surrogates to

reduce uncertainties in selecting the best surrogate and sampling strategy. We have also developed an averaging technique for multiple surrogates that protects against poor surrogates and performed at par with the best surrogate for many problems.

In this paper, we discuss the fundamental issues that arise in surrogate-based analysis and optimization, highlighting concepts, methods, and techniques, as well as practical implications. To aid the discussions of the issues involved, we will summarize recent efforts in investigating cryogenic cavitating flows, active flow control based on dielectric barrier discharge concepts, and lithium-ion batteries. In cavitating flows of cryogenic fluids, such as liquid nitrogen and hydrogen, thermal effects are very important. Surrogate-based analysis has been used to investigate the importance of two adjustable parameters, which regulate the strength of the evaporation and condensation rate in the cavitation model, and the sensitivity of the thermal-sensible fluid properties, including latent heat and vapor phase density. The surrogate-based strategy has also been used to establish appropriate values for these empirical constants. For the dielectric barrier discharge (DBD) actuator, the impact of the applied voltage frequency, the insulator dielectric constant and the polarity time ratio of the voltage waveform on the net force generation and required power are examined. Multiple surrogate models consistently identify two branches of the Pareto front where a positive x-directional net force requires relatively low power, while a negative net force requires high power. Moreover, global sensitivity analysis indicates that the voltage frequency and polarity time ratio are important in only some portions of the design space, while the dielectric constant is always important. A lithium-ion battery cell has also been analyzed using a surrogate modeling framework to map the effect of cycling rate, cathode particle size, and diffusion coefficient and electrical conductivity of the solid cathode material on the energy storage. Through global sensitivity analysis the relative impact of the various parameters can be quantified under different scenarios. The design space is split into distinct regions based on characteristic discharge and diffusion time scales for separate, more refined analysis. A Pareto front is constructed to quantify the tradeoff between maximum achievable energy and power levels.

The rest of the paper is structured as follows. We first present an overview of the surrogate methodology to highlight the key steps involved. Surrogate tools applied to cryogenic cavitation, flow control using DBD actuators, and lithium-ion battery cells are discussed next. We conclude the paper with a summary of key aspects of surrogate analysis that are common to all case studies presented and their relevance to other problems of multi-objective optimization.

SURROGATE MODELING METHODOLOGY

The key steps in the surrogate modeling process are shown in FIGURE 1. The process begins with constructing a set of experimental or numerical experiments, based on which surrogates are trained and refined.

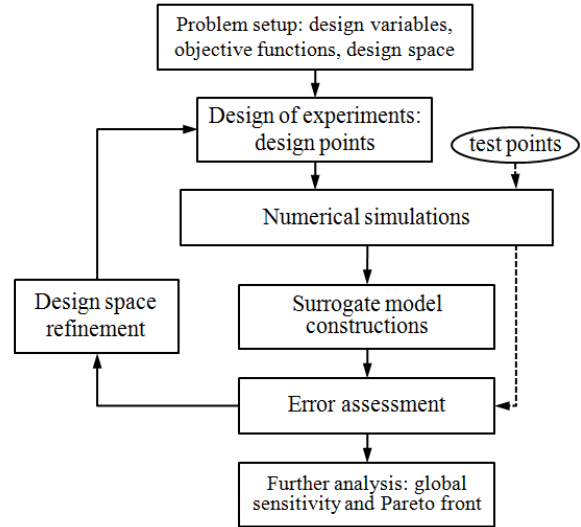


FIGURE 1. FLOWCHART FOR THE SURROGATE-BASED MODELING FRAMEWORK

Design of Experiments

The design of experiments consists of the design points at which training data for the surrogate models are obtained. In most problems the nature of the objective function is not known beforehand, so it may be simplest to use random sampling of the design space to avoid biased sampling. However, the number of experiments or simulations that can be conducted is often limited, so a more efficient approach is desired. One improvement over pure random sampling is Latin Hypercube sampling (LHS), which provides a random sampling but ensures a stratified sample within the full range of each dimension of the sample space [3].

Although LHS can give a representative sample design ranges, due to its random nature it does not ensure sampling the extrema of the parameter space, which may be of critical interest. One method considered in this study for sampling design space boundaries is the two-level face-centered composite design (FCCD), which includes the face-center points and vertices of the design hypercube [4].

Surrogate Models

In general, different types of surrogate models should be attempted and compared if possible, since the best method is problem-dependent (and, as will be seen, region-dependent within a single design space) and cannot be predicted beforehand. A brief description of the commonly used models is as follows; further details can be found in [Error! Reference source not found.].

Polynomial Response Surface (PRS). In a polynomial response surface model, the objective function is

approximated as a linear combination of polynomial basis functions:

$$\hat{y}(\mathbf{x}) = \sum_i b_i f_i(\mathbf{x}) \quad (1)$$

The number of i terms and the maximum degree of $f_i(\mathbf{x})$ are determined by the order of the PRS model. There often exists an ‘‘optimum’’ polynomial order; higher-order polynomial response surfaces can potentially achieve greater accuracy by allowing more degrees of freedom, but can also suffer from excessive curvature that can hinder accuracy and show inconsistent trends in the objective function from actual data. The coefficient vector \mathbf{b} is selected using a least squares method such that the prediction error at the training data points is minimized.

The adjusted coefficient of determination quantifies the prediction capability of the polynomial response surface approximation. This parameter is defined to account for the number of sample points:

$$R_{adj}^2 = 1 - \frac{\sigma_a^2 (N_s - 1)}{\sum_{i=1}^{N_s} (y_i - \bar{y})^2} \quad (2)$$

A good polynomial fit should have a small RMS error, and thus an R_{adj}^2 value close to 1.

Kriging (KRG). In a kriging model, the objective function is approximated as a sum of a polynomial regression model and a systematic departure $Z(\mathbf{x})$:

$$\hat{y}(\mathbf{x}) = \sum_i b_i f_i(\mathbf{x}) + Z(\mathbf{x}) \quad (3)$$

The systematic departure components are assumed to be correlated as a function of distance between the locations under consideration. In this study a variety of correlation functions are considered: Gaussian, linear, exponential, cubic, (cubic) spline, and spherical. A detailed formulation of these correlation functions has been summarized by Lophaven et al. [6].

Radial-Basis Neural Network (RBNN). A radial-basis neural network model approximates the objective function as a linear combination of radial basis functions [7], also known as neurons:

$$\hat{y}(\mathbf{x}) = \sum_{i=1}^{N_{RBF}} w_i a_i(\mathbf{x}) \quad (4)$$

The Gaussian function has been used as the radial basis function in this study:

$$a_i(\mathbf{x}) = e^{-\|\mathbf{s}_i - \mathbf{x}\|^{\beta}} \quad (5)$$

In Eqn. (5) the quantity $\|\mathbf{s}_i - \mathbf{x}\|$ is the distance to the i^{th} radial basis function. The number of neurons and associated weights are determined by satisfying the user defined error ‘‘goal’’ on the mean squared error in approximation.

PRESS Weighted Surrogates (PWS). Weighted average surrogate models combine information from multiple

individual surrogates via a weighting scheme to reduced uncertainties in selecting the best model based on limited validation criteria. Various weighting strategies are possible; we adopt a method based on the PRESS values of the individual surrogates. Further details of weighting strategies for multiple surrogates can be found in [8].

Cross-Validation

In order to select appropriate surrogate models for analysis, methods for evaluating and comparing the accuracy of the models are required. Procedures for comparing error measures for kriging and PRS models have been developed by Goel et al. [9]. One common strategy is to obtain simulation data at test points not used in the construction of surrogate models. The prediction error could then be computed at each test point for each surrogate model. While this method is easy to use and is useful for performing cross-validation, it is also limited by the number of test points that can be selected and the location of these points. The use of other cross-validation techniques in conjunction with test-point prediction error has also been adopted.

To estimate the accuracy of a surrogate model independent of test points, a parameter called the prediction error sum of squares (PRESS) can also be computed. PRESS is computed directly from the training data by summing the ‘‘leave-one-out’’ prediction errors at all data points. The ‘‘leave-one-out’’ prediction error is defined as the prediction error at a particular point using the surrogate model constructed from all other data points. In a more general formulation allowing an arbitrary number of data points to be left out at a time, this parameter is known as the generalized mean square error (GMSE). In this study, we use the PRESS (RMS) value as the basis of evaluation and comparison:

$$PRESS = \sqrt{\frac{1}{N_s} \sum_{i=1}^{N_s} (y_i - \hat{y}_i^{(-i)})^2} \quad (6)$$

In Eqn. (6), $\hat{y}_i^{(-i)}$ represents the prediction at $\mathbf{x}^{(i)}$ using the surrogate constructed using all sample points except $(\mathbf{x}^{(i)}, y_i)$.

Global Sensitivity Analysis

Global sensitivity analysis can be useful for comparing the relative magnitude of effect of the design variables on the objective function, especially if the number of design variables is large. Variables that have little effect on the objective function can be identified and removed from consideration, allowing the design space to be reduced. A method similar to that used by Sobol [10] has been employed in this work.

An objective function f (obtained from the surrogate model) can be decomposed as a sum of functions of individual variables and combinations of variables, known as additive functions:

$$f(\mathbf{x}) = f_0 + \sum_i f_i(x_i) + \sum_{i < j} f_{ij}(x_i, x_j) + \dots \quad (7)$$

$$+f_{1\dots N_v}(x_1, \dots, x_{N_v})$$

The total variance $V(f)$ is defined as the expected value of the square of the summation of all non-zero order additive functions. The total variance can also be expressed as a sum of partial variances of the individual variables and combinations of variables:

$$V(f) = \sum_{i=1}^{N_v} V_i + \sum_{i<j} V_{ij} + \dots + V_{1\dots N_v} \quad (8)$$

The partial variances are in turn defined in terms of the expected value of the additive functions:

$$V_i = V(E[f | x_i])$$

$$V_{ij} = V(E[f | x_i, x_j]) - V_i - V_j \quad (9)$$

The expected values of the additive functions and their variances can be expressed as integrals of the additive functions which are approximated using a five point Gauss quadrature scheme in this study:

$$E[f | x_i] = \int_0^1 f_i dx_i \quad (10A)$$

$$V(E[f | x_i]) = \int_0^1 f_i^2 dx_i \quad (10B)$$

The main sensitivity indices can then be computed from the partial variances:

$$S_{Mi} = \frac{V_i}{V(f)} \quad (11)$$

The total sensitivity index for the i^{th} variable is defined as the sum of all variance terms involving i , divided by the total variance. This can be expressed as a sum of the main sensitivity index and all higher-order terms involving i :

$$S_{Ti} = S_{Mi} + \frac{\sum_{j, j \neq i} V_{ij} + \dots}{V(f)} \quad (12)$$

The relative importance of the design variables can be observed by comparing either their partial variances (main sensitivity indices) or their total variances (total sensitivity indices). The difference between the main and total sensitivity indices for each variable also gives an indication of the degree of interaction between variables.

Pareto Front

A single continuous objective function obtained through surrogate-based modeling may be further optimized by simply searching the design space for the minimum or maximum value of the objective. However, if multiple competing objectives are present, there may be no single optimal design, but many designs in which one objective is improved at the cost of another [11]. Pareto-optimal solutions (also known as Pareto-efficient solutions) comprise the set of designs that are not dominated by any other design. A design is said to be dominated by another if it is no better in any objectives, and worse in at least one objective. The set of Pareto-optimal solutions can be used to construct a Pareto front, which

represents all optimal combinations of the objectives if their relative importance is not known. In the surrogate modeling framework, a surrogate model can also be utilized to construct the Pareto front in addition to the existing training data. Inspection of the Pareto front may then reveal the existence of favorable tradeoffs between the competing objectives, and assist significantly in the optimization process.

CASE STUDIES TO DEMONSTRATE SURROGATE MODELING TECHNIQUES

Having introduced the methodology and basic concepts, we now present different scenarios where the surrogate-based modeling and optimization has been used to study the interplay of independent variables and their influence on the desired objective(s) for cases that include cavitation in cryogenic fluids, dielectric barrier discharge actuator and modeling of lithium-ion cells. A brief overview of the motivation and methods used in each study has been outlined, followed by a discussion of the key findings and summary of the contributions provided by the surrogate-based framework.

Cavitation in Cryogenic Fluids

Cryogenic liquids, including liquid oxygen, nitrogen, and hydrogen, are used as liquid rocket propellants due to their high power density and clean by-products. A key design issue surrounding rocket fuel and oxidizer pumps is the minimum pressure that the design can tolerate for a given inlet temperature and rotational speed. To keep inlet pressure low (reducing tank weight) and pump rotational speeds high (reducing engine weight), cavitation, which occurs when the local pressure in a fluid is lower than the vapor pressure [Error! Reference source not found.-Error! Reference source not found.], is prone to appear in the inducer section. When this occurs, the forming vapor phase will replace the liquid inside the cavity; in order to maintain the vapor phase, the surrounding liquid will adjust its thermodynamic state and experience evaporative cooling, causing a temperature drop in the surrounding area. Although various cavitation models have been categorized and documented, for example in ref. [Error! Reference source not found.-Error! Reference source not found.], there is, to date, no established method capable of predicting the actual loads due to cavitation on the inducer blades. The unsteadiness of the cavitating pump can be coupled with the feed or discharge system, causing large component oscillations. Furthermore, thermal effects are much stronger in cryogenic cavitating liquids than in conventional liquids such as water due to the thermal-sensibility of properties such as vapor pressure and reduced liquid-vapor density ratios under such conditions [Error! Reference source not found.].

Due to the complexity of the flow phenomena, validated computational tools capable of predicting cavitating flow behavior are necessary for rocket fuel-oxidizer pump design. In this study we seek to use surrogate modeling tools to assess and improve the predictive capabilities of a cavitation model with

respect to model parameters by comparing the output to experimental data.

Physical Model. The Navier-Stokes equations are well established for multi-phase fluid dynamics. The set of governing equations for the cavitation computation under the homogeneous-fluid modeling consists of the conservative form of the Favre-averaged Navier-Stokes equations, the enthalpy-based energy equation for cryogenic cavitation, the $k-\varepsilon$ two-equation turbulence closure, and a suitable cavitation model. The details are well-documented in ref. [18-22]. Generally, a cavitation model is a transport equation for the liquid volume fraction α_l , which can be written in the following form:

$$\frac{\partial(\alpha_l)}{\partial t} + \frac{\partial(\alpha_l u_j)}{\partial x_j} = m^+ + m^- \quad (13)$$

Fluid mixture properties, such as mixture density, can be evaluated based on the liquid volume fraction, vapor phase density ρ_v , and liquid phase density ρ_l :

$$\phi_m = \phi_l \alpha_l + \phi_v (1 - \alpha_l) \quad (14)$$

The source (m^+) and sink (m^-) terms in Eqn. (13) correspond to the condensation and evaporation rates, respectively. Multiple studies documented in ref. [Error! Reference source not found.-Error! Reference source not found.] have modeled the liquid volume fraction α_l (or vapor volume fraction) via the sink and source terms, which regulate the mass transfer between vapor and liquid phases with empirical constants. Liquid-vapor evaporation and condensation rates for this transport-based cavitation model can be written in the following form:

$$\begin{aligned} m^- &= \frac{C_{dest} \alpha_l \rho_l \min(0, P - P_v)}{t_\infty \rho_v (0.5 \rho_l U_\infty^2)} \\ m^+ &= \frac{C_{prod} (1 - \alpha_l) \max(0, P - P_v)}{t_\infty (0.5 \rho_l U_\infty^2)} \end{aligned} \quad (15)$$

In Eqn.(15), P is the local pressure and P_v is the vapor pressure. U_∞ is the reference velocity scale, and t_∞ is the reference time scale, defined as the characteristic length scale D divided by the reference velocity scale. The conditional statements in the source and sink terms indicate that evaporation occurs when the pressure is less than the vapor pressure, and that condensation occurs when the pressure is greater than the vapor pressure, under the assumption of thermal equilibrium. Based on current flow conditions, the cavitation is attached, and hence the steady-state calculation is used. Note that in addition to the fluid properties and flow parameters, Eqn. (15) also relies on two empirical constants, C_{dest} and C_{prod} . Furthermore, C_{dest} and C_{prod} are material dependent constants [Error! Reference source not found.-Error! Reference source not found.].

In the case of cryogenic cavitation, the thermal effects cannot be neglected and an additional equation is required:

$$\frac{\partial}{\partial x_j} [\rho_m u_j (h + f_v L)] = \frac{\partial}{\partial x_j} \left[\left(\frac{\mu_L}{Pr_L} + \frac{\mu_T}{Pr_T} \right) \frac{\partial h}{\partial x_j} \right] \quad (16)$$

Note in Eqn. (16) that the subscripts L and T indicate laminar and turbulent flow, respectively. The temperature T can be computed based on the enthalpy h [Error! Reference source not found.], and the vapor mass fraction is expressed as:

$$f_v = \frac{\rho_v (1 - \alpha_l)}{\rho_m} \quad (17)$$

In summary, this homogeneous fluid cavitation model consists of the conservative form of the Favre-averaged Navier-Stokes equations, the enthalpy-based energy equation for cryogenic cavitation, the $k-\varepsilon$ two-equation turbulence closure based on a filter approach [Error! Reference source not found.-Error! Reference source not found.], and a transport equation for the liquid volume fraction. More details of cavitation modeling can be found in ref. [Error! Reference source not found.-Error! Reference source not found.].

In this study, we use surrogate modeling techniques to assess the influence of parameters regulating the condensation and evaporation rates and uncertainties in material properties on the performance of the transport-based cryogenic model.

Surrogate Modeling Process. (a) Design of Experiments and Cross-Validation: In this study we consider cryogenic cavitation with thermal effects in a 2D domain. A schematic of this problem setup is illustrated in FIGURE 2. Two cases corresponding to experimental data reported in ref. [24] are investigated with the conditions listed in TABLE 1. In both cases the working fluid is liquid nitrogen, and the computational domain consists of 2×10^4 structured grid elements.

TABLE 1. CRYOGENIC CAVITATION CASES CONDITIONS

CASE	290C	296B
σ_∞	1.7	1.61
Re	9.1×10^6	11.0×10^6
T_∞	83.06 K	88.54 K

Since we wish to assess the overall predictive performance of the cavitation model, the objective functions of interest are the RMS values of the differences between computed and experimental [24] temperature (T_{diff}) and pressure (P_{diff}) values, evaluated at five different locations along the hydrofoil surface shown in FIGURE 2.

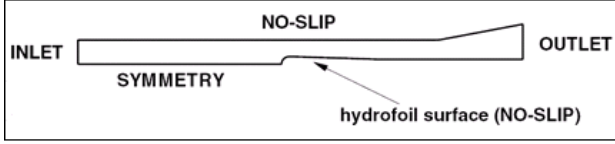


FIGURE 2. SCHEMATIC OF THE GEOMETRY AND BOUNDARY CONDITIONS

TABLE 2 lists the design variables considered and their ranges, as well as the objective functions. The ranges of the two empirical constants C_{dest} and C_{prod} , which directly control the evaporation and condensation rates in the cavitation model, are selected in accordance with those found in ref. [24]. The effects of perturbations in the fluid properties are also examined by varying the vapor density, which dominates the evaporating cooling term and also appears directly in the cavitation sink term, and latent heat, which determines the energy absorbed or released during the phase change, relative to the NIST database values [17].

TABLE 2. OBJECTIVE FUNCTIONS AND DESIGN VARIABLES WITH CORRESPONDING RANGES

SYMBOL	DESIGN VARIABLE	RANGE
C_{DEST}	EVAPORATION RATE	0.578~0.68
C_{PROD}	CONDENSATION RATE	46.2~54.4
P_V	VAPOR DENSITY*	-10%~10%
L	LATENT HEAT*	-10%~10%
SYMBOL	OBJECTIVE FUNCTION	
P_{DIFF}	PRESSURE DIFFERENCE BETWEEN CFD AND EXP. DATA	
T_{DIFF}	TEMPERATURE DIFFERENCE BETWEEN CFD AND EXP. DATA	

*: Vapor density and latent heat are relative to database values.

FIGURE 3 shows the sensitivity of T_{diff} and P_{diff} with respect to the empirical constants for Case 290C without perturbations in material properties. Case 296B also shows similar results. Clearly, the temperature and pressure distribution shows some dependence on the empirical constant values, so no immediate reduction in problem dimensionality is

available. An example of a cavity outlook ($C_{dest} = 0.639$, $C_{prod} = 54.4$) is also shown in FIGURE 3 (c).

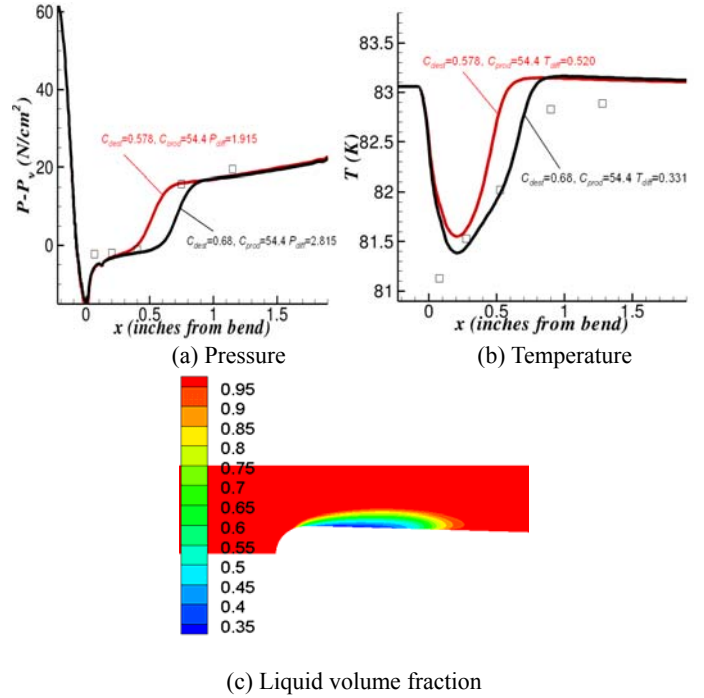


FIGURE 3. CRYOGENIC CAVITATION CASES Case 290C ($\sigma_\infty = 1.7$, $Re = 9.1 \times 10^6$, $T_\infty = 83.06$ K)

TABLE 3. CROSS-VALIDATION MEASURES FOR SURROGATES (70 TRAINING POINTS)

Surrogate	P_{diff}^*		T_{diff}^*	
	290C	296B	290C	296B
PRESS (PRS)	6.38%	11.90%	9.11%	10.02%
R^2_{adj} (PRS)	0.962	0.939	0.892	0.928
PRESS (KRG)	2.97%	2.93%	2.48%	6.62%
PRESS (RBNN)	13.91%	11.67%	13.31%	19.03%
PRESS (PWS)	3.97%	5.44%	5.50%	9.20%

A design experiments consisting of 70 training data points is selected using a combined FCCD strategy (25 points) and LHS (45 points). PRS, KRG, RBNN, and PWS models of both objectives in normalized variable space are constructed, and objective function values are also normalized. Second order polynomials for PRS and spread coefficients in the range between 0.4 and 0.7 are considered.

Cross-validation measures are summarized in Tab. 3. Based on the PRESS criterion, the KRG model is found to have

the best overall performance while the RBNN has the worst. Five additional independent test points are also considered for cross-validation; the KRG model also shows the best agreement for both Case 290C and 296B in ref. [24]. Based on these cross-validation results, the KRG model is selected for global sensitivity analysis.

(b) Global Sensitivity Analysis: FIGURE 4 and FIGURE 5 show the overall impact of each design variable on both objectives for Case 290C and 296B, respectively. The overall sensitivity results are similar for the pressure prediction in the two cases, where the effects of the evaporative and vapor density terms are very important while the contributions from the condensation and latent heat terms are much less significant. However, the effect of latent heat on the temperature distribution is much more significant in Case 296B than in Case 290C. Since Case 296B has a greater inlet temperature, this suggests that the sensitivity of the thermal field to thermodynamic properties increases with temperature. In both cases, the condensation term has negligible influence on both objectives, allowing a reduction in problem dimensionality.

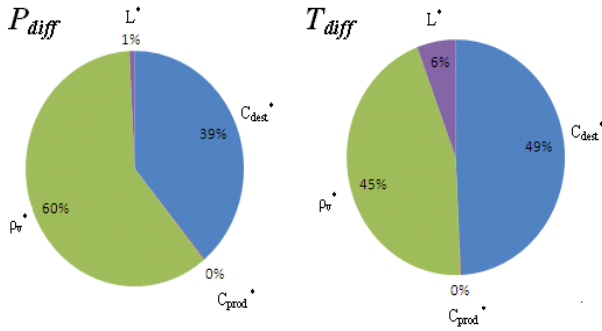


FIGURE 4. GLOBAL SENSITIVITY INDICES FOR CASE 290C

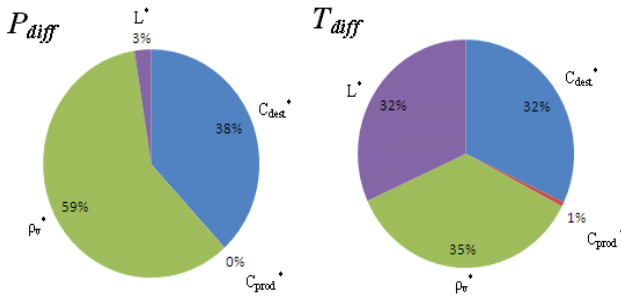


FIGURE 5. GLOBAL SENSITIVITY INDICES FOR CASE 296B

(c) Dimensionality Reduction: In the next step of the surrogate process, we can optimize the evaporative term C_{dest} within its design range to minimize the pressure and temperature discrepancies between computed results and experimental data. Since the condensation term does not influence the performance of the present cryogenic cavitation model, it is

appropriate to fix its value ($C_{prod} = 54.4$). Additionally, since material properties are not variables that can be tuned for optimization and are studied only to compare the relative sensitivity of the pressure and temperature distribution to uncertainties in these properties, we fix the temperature-dependent material properties ρ_v and L to values obtained from the NIST database [17].

The two objectives are plotted against the evaporative term for both cases in FIGURE 6. Note that while in Case 296B the two objectives show a similar trend to each other, they show very different trends in Case 290C. Due to these opposing trends, the optimal value for C_{dest} depends on which objective should be minimized. Instead of a single optimum, there exists a Pareto-optimal set of solutions among which one objective may only be improved at the cost of the other.

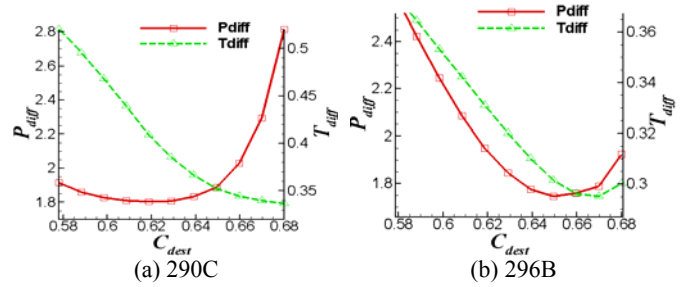


FIGURE 6. LOCATION OF POINTS (C_{dest}) AND CORRESPONDING RESPONSES (P_{diff} IS SHOWN ON THE LEFT Y-AXIS, AND T_{diff} IS SHOWN ON THE RIGHT Y-AXIS) USED FOR CALIBRATION OF THE CRYOGENIC CAVITATION MODEL

(d) Multiobjective Optimization: Tradeoffs between the two objectives for both cases are plotted in FIGURE 7.

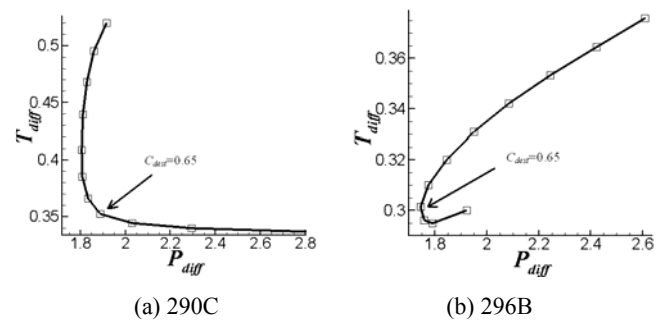


FIGURE 7. PARETO FRONTS SHOWING TRADEOFFS BETWEEN OBJECTIVES FOR BOTH CASES

Despite the similar trends in the two objectives in Case 296B as shown in FIGURE 6(b),

FIGURE 7(b) shows that there also exists a Pareto-optimal set, although much smaller than in Case 290C. Note that in Case 290C, significant reductions in P_{diff} can be realized while incurring a small penalty in T_{diff} . Combined with the fact that

pressure fluctuations play a more important role in determining the cavitation dynamics and the loadings on fluid machinery, this nonlinear tradeoff strongly favors reducing P_{diff} , suggesting an optimal value of about $C_{dest} = 0.65$, which also coincides with one of the Pareto-optimal solutions in Case 296B. This is also the value used for other liquid nitrogen cases in ref. [24], suggesting that the optimum is insensitive to differing thermal effects, since these cases correspond to different operating temperatures.

This exercise has helped to validate the model parameter values. Note that since the model parameters are material dependent, the optimal evaporative parameter will vary with different cryogenic fluids. For example, repeating the process with liquid hydrogen showed that the optimal value should be $C_{dest} = 0.78$.

Major Outcome. To assess the effects of model parameters and material property uncertainties on the predictive performance of the cryogenic cavitation model, we select C_{dest} , C_{prod} , ρ_{vs} , and L as design variables and computed predictive errors in the pressure (P_{diff}) and temperature (T_{diff}) distribution. The KRG model is found to be the most suitable surrogate model due to its PRESS value and independent test point prediction. Global sensitivity analysis shows that the performance of the current cavitation model is affected most by the evaporative and vapor density terms, while the condensation term is not important at all within this design space, and the latent heat is significant only in temperature prediction. This enabled a reduction in the problem dimensionality, allowing the evaporative term to be optimized to minimize prediction error of the cavitation model when compared to experimental data. Although a Pareto front is found demonstrating tradeoffs between the pressure and temperature prediction, we recommend a value of $C_{dest} = 0.65$ due to the large gains available in pressure prediction at a small sacrifice in temperature prediction. Furthermore, this optimum is not affected by the different thermal effects from our current selected cases.

Dielectric Barrier Discharge for Flow and Thermal Management

The DBD plasma actuator is a flow control device that is comprised of two asymmetrically placed electrodes separated by a dielectric barrier (insulator) and driven by the kilohertz radio frequency AC or pulses with kilo-volt amplitude as shown in **FIGURE 8**. The discharge generates a weakly ionized gas and charged particles influenced by the electric field can deliver momentum to the neutral particles [25],[26]. Asymmetric geometry and charged particle dynamics, as a result, contribute to generate a unidirectional wall jet type flow [27],[28].

In spite of the inherent advantages (no moving parts and vast control potential) of the DBD actuator, little insight is available regarding efficient operating conditions to accommodate various performance needs. With relatively high magnitudes of applied voltage (15 kV at 5-10kHz AC) required

for a uniform discharge, the force per unit width generated by a single actuator is less than 10 mN/m in air [29]. The flow velocity induced by a single actuator is usually less than 5m/s for pulsed input voltage [30] as well as sinusoidal voltage waveforms [31]. In their efforts to understand the operating mechanism and possible optimal conditions for the actuator, various researchers have conducted parametric studies in terms of the waveform and frequency of the applied voltage, actuator geometry, and dielectric constant [31]-[33].

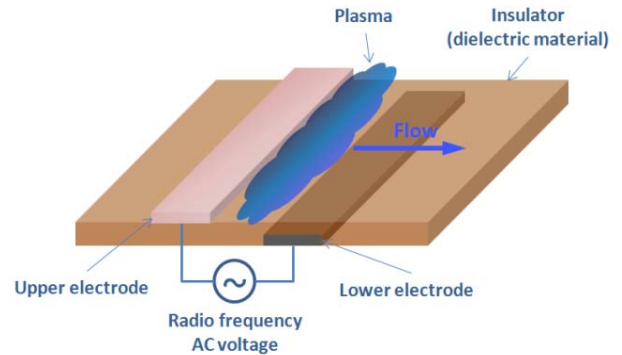


FIGURE 8. DIELECTRIC BARRIER DISCHARGE ACTUATOR CONFIGURATION

The present study focuses on understanding the effect of three chosen parameters – waveform and frequency of the applied voltage and dielectric constant of the insulator – on the DBD actuator performance characterized by power input and generated flow directional force using surrogate models. The main objective is to assess the importance and impact of those variables, which have significant interplay on the actuator performance. The accuracy of each surrogate model for this application is also addressed and the surrogate models with reasonable accuracy are shown to contribute to successfully refining the design space, resolving the region of interest with higher accuracy.

Physical Model. The DBD actuator is modeled with the continuity and momentum, and electric field equations derived from the Boltzmann and Maxwell’s equations, respectively. Since the atmospheric pressure is sufficiently high to assume local thermodynamic equilibrium, the fluid model is reasonably accurate and the local electric field density (E/N) can be used to approximate the phenomena related to the collision processes – ionization/recombination, diffusion and drift - instead of solving the energy equation [34]. Governing equations are given as Eqns. (18) to (20) for only two species – He^+ (subscript $p = i$) and electron (subscript $p = e$) – for simplicity in this paper. S_{ie} and r are ionization and recombination rate coefficients, and μ and D are mobility and diffusivity of charged particles, respectively. q is electric charge of one species particle, and ϵ_0 is permittivity of vacuum.

$$\frac{\partial n_p}{\partial t} + \nabla \cdot (n_p \mathbf{u}_p) = n_e S_{ie} - r n_i n_e \quad (18)$$

$$n_p \mu_p \mathbf{E} - \nabla (n_p D_p) = n_p \mathbf{u}_p \quad (19)$$

$$\nabla \cdot (\epsilon_d \mathbf{E}) = \frac{q_i n_i - q_e n_e}{\epsilon_0} \quad (20)$$

Equation (19) is the well-known drift-diffusion equation, which is valid also for ions in high pressure (atmospheric regime) discharge. To solve this set of equations, the source terms are handled with 4th order backward differentiation formula (BDF) and the Poisson equation with the algebraic multigrid method, and the second-order central difference and upwind methods are employed for the diffusion and convection terms respectively [35]. The charged particle densities and electric field are coupled by solving the Poisson equation between the predictor and corrector steps where the first order source splitting is used as noted in [34]. The coefficients of gaseous properties of helium regarding particle collisions and ionization/production are obtained from [25][26],[36].

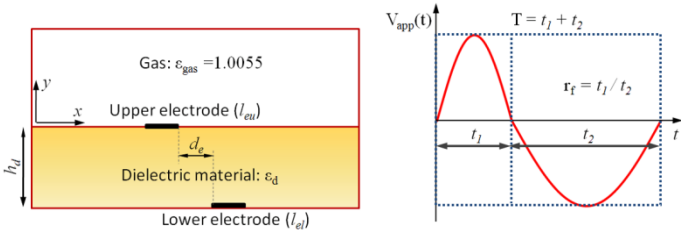


FIGURE 9. COMPUTATIONAL DOMAIN AND APPLIED WAVEFORM

The computational domain with the actuator geometry is presented in **FIGURE 9**. The thickness of the insulator (h_d) is set as 0.5cm and the lengths of upper (l_{eu}) and lower electrodes (l_{el}) are 0.2 cm same as the gap distance (d_e). The applied voltage to the upper electrode has sinusoidal shape with 1 kV amplitude but the positive-to-negative half cycle ratio r_f can be varied. Boundary conditions for the charge species at the dielectric surface are set to satisfy the current continuity that allows the accumulation of particles, and only electrons are allowed to be absorbed in the upper electrode without the secondary emission. Gas pressure of helium is set as 300 mmHg, and the ion temperature is 300K. The electron temperature is calculated as a function of the local electric field strength using a local field approximation approach, which is discussed in detail in [35].

Surrogate Modeling Process. (a) **Design of Experiments and Cross-Validation:** Among the many possible parameters affecting the actuator performance, three are chosen as design variables to assess their impact on the actuator efficiency. The dielectric constant of the insulator

material (ϵ_d), frequency of the applied voltage (f_v) and positive-to-negative half cycle ratio (r_f) are chosen for this study because they are among the key parameters which have non-simple effects on the resultant force by affecting both of the positive and negative peak value of domain averaged force and asymmetry in its waveform [37]. The constraint of each design variable is devised by considering the existing choice of materials and the general working conditions of previous DBD actuators. The objective functions are chosen to represent the actuator performance, namely the time and domain averaged x-directional force ($F_{x,ST}$) and average power input to the circuit (P_T) based on the charge current through the upper electrode. The time and domain averaged Lorentzian force to the charged particles is assumed to be equivalent to the body force acting on the neutral gas, especially at atmospheric pressure conditions. The definitions and parameter ranges are presented in **TABLE 4**.

TABLE 4. DESIGN VARIABLES, CONSTRAINTS, AND OBJECTIVE FUNCTIONS

Symbol	Design variable	Constraint
ϵ_d	Dielectric constant of insulator	$2 \leq \epsilon_d \leq 15$
f_v	Frequency of the applied voltage (kHz)	$5 \leq f_v \leq 20$
r_f	Positive-to-negative half cycle ratio	$0.5 \leq r_f \leq 1.5$
Symbol	Design variable	Definition
$- F_{x,ST} $	Time and domain averaged x-directional force (mN/m)	$F_{x,ST} \equiv \frac{1}{ST} \int_S \int_T F_x(\bar{r}, t) dt d\bar{r}$
P_T	Power input for one cycle by the charge current through the upper electrode (W)	$P_T \equiv \frac{1}{T} \int_T I(t) V(t) dt$ where $I(t) \equiv \int_{l_{eu}} (q_i n_i(t) u_{y,i}(t) - q_e n_e(t) u_{y,e}(t)) dx$

The first level design of experiments, level 0 using the combination of 15 FCCD points and 5 LHS points and the simulation result of ϵ_d for those 20 points are presented in **FIGURE 10**. Although the sampled points are well distributed in

the design space, the response points cluster in some parts of the response space as in **FIGURE 10**.

The surrogate models are obtained using these sampled points and their PRESS errors are presented in **TABLE 5**. Due to the insufficient number of sampled points and their complex response, significant PRESS errors exist at this level especially in force prediction. For this case the KRG model shows the best performance in predicting the force while the parameter-based average model does the same for power.

In order to explore the objective function distribution corresponding to the design space, a grid with 31^3 points evenly distributed in the whole design space is employed, and the result using the PWS is presented in **FIGURE 11**. It can be observed that the Pareto front is not continuous and there are two distinct regions that are marked with two windows and correspond to the higher magnitude of force generation. Though they both lie in the same side of the force axis due to our adopting the absolute values of the force, the one with higher power corresponds to the negative (minus x-direction in **FIGURE 9**) force generation, and the lower to the positive. On the other hand, the region corresponding to the positive force generation ensures a gain in force generation with much lower power.

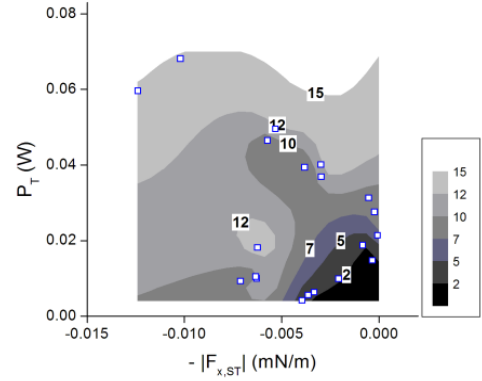


FIGURE 10. CONTOURS OF ε_d WITH SIMULATION RESULTS IN OBJECTIVE FUNCTION SPACE IN LEVEL 0

TABLE 5. PRESS ERRORS OF THE SURROGATE MODELS IN LEVEL 0

	$- F_{x,ST} $	P_T
KRG	0.0020 (16)*	0.0032 (5.0)
PRS	0.0027 (22)	0.0033 (5.2)
RBNN	0.0095 (77)	0.0063 (9.9)
PWS	0.0028 (23)	0.0023 (3.6)

*: () % = $100 \times \text{PRESS} / (X_{\max} - X_{\min})$, $X = -|F_{x,ST}|$ or P_T in level 0.

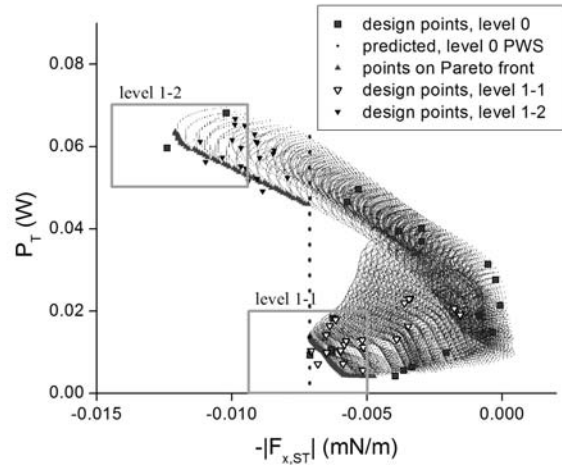


FIGURE 11. DESIGN AND PREDICTED POINTS AND PARETO FRONTS BY THE PRESS WEIGHTED SURROGATES IN LEVEL 0

In **FIGURE 11**, since the distribution of sampled points near the Pareto front are too sparse to resolve the regions of interest properly, two windowed regions are used as the constraints for design space refinement.

Level 1-1, low power region:

$$-0.009 \leq -|F_{x,ST}| \leq -0.005 \text{ [mN/m]}, \quad 0 \leq P_T \leq 0.02 \text{ [W]}$$

Level 1-2, high power region:

$$-0.014 \leq -|F_{x,ST}| \leq -0.009 \text{ [mN/m]}, \quad 0.05 \leq P_T \leq 0.07 \text{ [W]}$$

The design variable constraints corresponding to these objective function constraints, namely design-space-constraints are generated based on the surrogate models at level 0. In order to generate the constraint surfaces, responses of a set of grid points uniformly distributed in the design space are obtained by using the surrogate models, and the surfaces confining the points whose responses satisfy the objective function constraints are then specified. Although the PWS has a smaller PRESS error in P_T as presented in **TABLE 5**, the design space confined by its design-space-constraints is included in that of the KRG model, and the refined regions are chosen conservatively to cover as much space as possible.

FIGURE 12 shows the iso-force and iso-power surfaces and the design-space-constraint surfaces based on the KRG model (blue is for the lower bounds and red the upper bounds). Considering the lower and upper bounds of the objectives, each level has one refined space along with constraint surfaces. Since these surfaces are contours of constant force or power, based on their slopes it can be said that the force generation is relatively less sensitive to the dielectric constant than power.

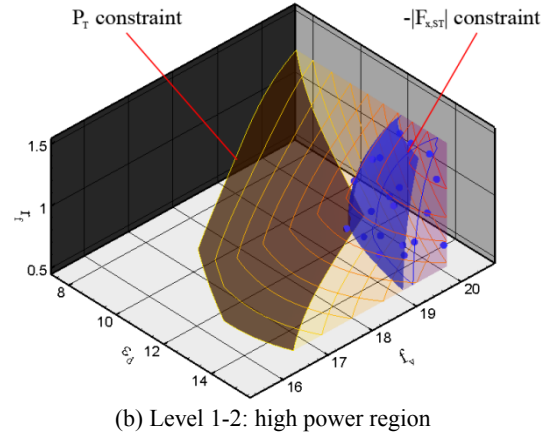
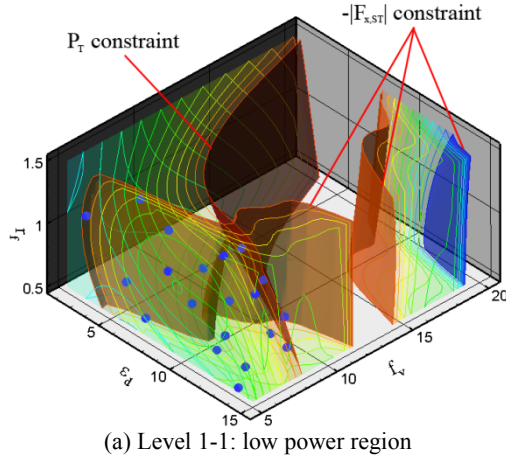
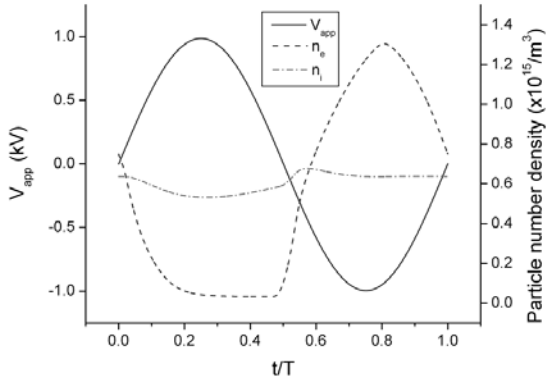


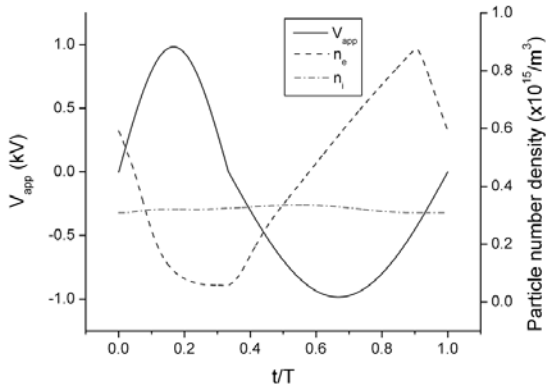
FIGURE 12. CONSTRAINTS, CONTOURS AND DESIGN POINTS FOR DESIGN SPACE REFINEMENT

Since the design space corresponding to level 1-1 and 1-2 constraint windows is irregular in shape, it is impossible to use the design of experiments for a rectangular hexahedron or sphere. For the design of experiments at the refined level, in order to sufficiently characterize the design space, the LHS is utilized to generate 5000 points. Then, 20 points are selected by maximizing the minimum distance between those points. The design points generated by this approach are also shown in **FIGURE 12** along with the constraint surfaces.

(b) Multiobjective Optimization: To investigate the phenomena in the high- and low-power regions in depth, two points corresponding to the minimum $-|F_{x,ST}|$ condition are selected and the time history of the solution is compared in **FIGURE 13** and **FIGURE 14**. In **FIGURE 13(a)** and **(b)** it can be observed that for the case with lower frequency that belongs to the low power region, domain-averaged ion number density is higher. This can be explained by considering the fact that lower frequency allows more time to generate the particles, which is consistent with that found in [37]. The electron saturation instances in these cases – about $t/T = 0.8$ in the low power and 0.9 in the high power – coincide with the start of plateau or second dip in **FIGURE 14**, which is also mentioned as one of the key factors affecting the solution with frequency.



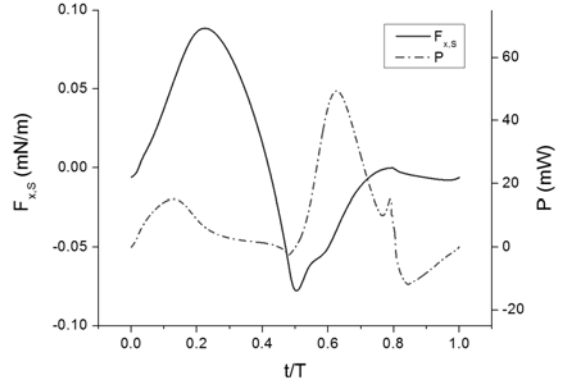
(a) Low power region: $\epsilon_d=8.5, f_v=5.0, r_f=1.0$



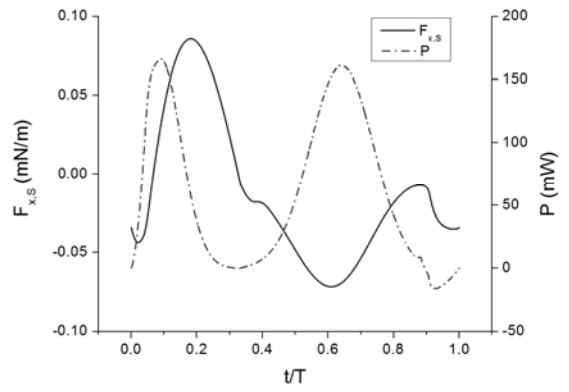
(b) High power region: $\epsilon_d=15.0, f_v=20.0, r_f=0.5$

FIGURE 13. DOMAIN-AVERAGED PARTICLE NUMBER DENSITY HISTORIES FOR TWO DESIGN POINTS NEAR THE PARETO FRONT

From the force history results, one can deduce the effect of the ratio of first and second half cycles, r_f . Although positive force belongs to the first half cycle and negative to the second, elongating the period of each part in the applied voltage source does not necessarily induce increased force either in positive or negative. While decreasing r_f , i.e. increasing the second half cycle corresponds to the decreased $-|F_{x,S7}|$ point in the high power region, increasing r_f does not mean increasing the duration of positive force cycle. The value of r_f corresponding to the maximum force generation in the positive x-direction is about 0.8 in the low power region according to the multiple surrogate model. The reason is that generating the positive force is mainly related to the plateau region of the second half cycle in $F_{x,S}$ time history as in **FIGURE 14**.



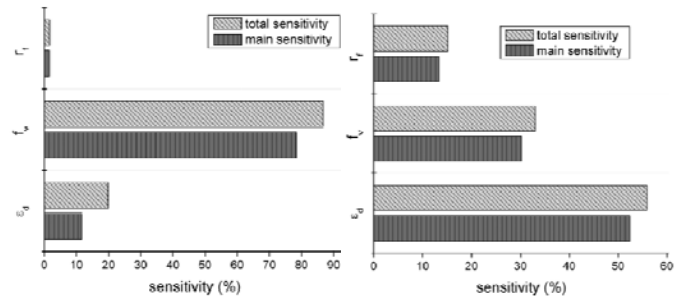
(a) Low power region: $\epsilon_d=8.5, f_v=5.0, r_f=1.0$



(b) High power region: $\epsilon_d=15.0, f_v=20.0, r_f=0.5$

FIGURE 14. FORCE AND POWER HISTORIES FOR TWO DESIGN POINTS NEAR THE PARETO FRONT

(c) Glogal Sensitivity Analysis: **FIGURE 15** shows the result of the variance-based, non-parametric global sensitivity analysis for each refined level. Compared to the level 1-2, level 1-1 shows a stronger parameter correlation, which can be identified from the difference between total and main sensitivities. Also, the frequency of applied voltage, f_v in level 1-1 has a significant effect on both the average force and power. On the other hand, in the high power region (level 1-2) the effect of the positive-to-negative time ratio, r_f is prominent compared to that of f_v , while the insulator dielectric constant is always important.



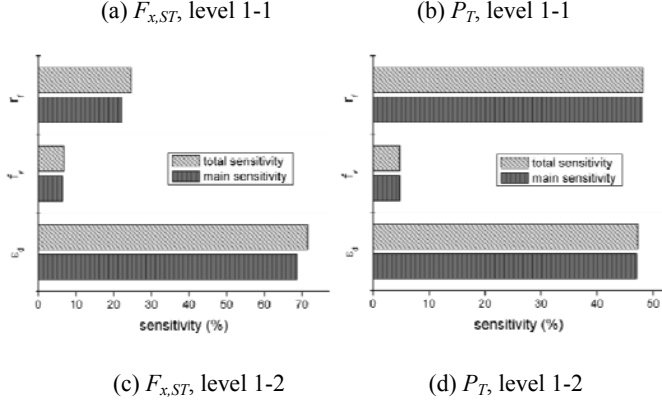


FIGURE 15. GLOBAL SENSITIVITY INDICES FOR THE AVERAGE FORCE AND POWER

Major Outcome. Multiple branches of Pareto front within two regions apart from each other in the original design space are observed. In these low and high power regions, the orientation of the time-averaged force, and degree of correlation and global sensitivity of design variables are very different. The results can be used to enhance the performance of the actuator by devising effective control variables and understanding their influence on performance. The major impacts of design variables on the objectives are summarized below.

The dielectric constant of the insulator affects the amount of charged particle clouds above the insulator wall during the second half cycle. With a smaller constant, particle clouds thicken, increasing the asymmetry between the two half cycles. As a result the average force, F_x increases. On the other hand it also affects the density of the charged particle layer on the insulator surface. With a larger constant, a higher electric field is produced, resulting in increase of F_x magnitude, but along the negative direction.

The applied voltage frequency affects the amount of overall charged particle generation. With a higher frequency, the discharge duration decreases and the asymmetry between the two half cycles decrease, resulting in larger F_x along the negative direction. Higher frequency accompanied by high dielectric constant induces larger power usage.

The positive-to-negative half cycle time ratio also contributes to the overall charged particle generation. With a larger ratio, the first half cycle discharge becomes more prominent. As a result, F_x increases. On the other hand, the amount of charged particle clouds above the insulator wall during the second half cycle is also influenced. The larger ratio induces a smaller level of charged particle generation, which means insufficient electric field for the plateau region in the second half cycle. As a result F_x decreases.

Having demonstrated the use of global sensitivity analysis and Pareto fronts for mapping the design space in the preceding case studies, we conclude with a study on the modeling of lithium ion battery cells, where a reduction in problem

dimensionality is shown to provide significant performance gains for the surrogate model.

Lithium-ion Battery Modeling

Lithium-ion batteries offer distinct advantages over other battery technologies due to their high energy density and low weight. However, despite significant experimentation and modeling effort, the competing effects of operational, geometric, and material parameters on battery performance are still not well understood. This may be attributed in part to the disparity in the measurement of material properties, such as the diffusion coefficient and electronic conductivity of the active materials, as well as the large number of variables and the difficulty of tuning them for experimental studies. Although various parametric studies have examined the role of individual design variables on cell performance capabilities, the combined effects of simultaneously varying several design variables and the relative magnitudes of their influence have not been established. Cross-interactions between variables are especially important as they may be responsible for critical design regions that cannot be identified by adjusting individual variables. These critical design regions are particularly useful in battery design due to the aforementioned limited ability to tune certain material properties, as well as the varying discharge rates experienced in the cell during operation.

Due to these considerations, as well as the fact that there are often multiple competing objectives such as gravimetric and volumetric energy density, power, and cycle life, a comprehensive examination and comparison of the role of various design variables on cell performance requires a systematic, efficient mathematical framework. In this study, we seek to use surrogate-based analysis tools to construct models that can efficiently and accurately predict the specific energy and power of a lithium-ion cell with respect to the cycling (or discharge) rate and the size and ion diffusivity and electronic conductivity of the active solid material. These models can thus be used to conduct global sensitivity analysis to identify critical design thresholds, observe combined effects due to cross-interactions, and quantify the relative importance of various parameters under different scenarios. An improved understanding of the most important performance-limiting factors will ultimately aid in cell optimization.

Physical Model. In this study, the discharge process of a cell consisting of an MCMB 2528 graphite anode and a lithium manganese oxide (spinel) cathode is modeled using a porous electrode formulation. In this model, the continuum-scale governing equations are solved in a pseudo-2D domain spanning the thickness of the cell and including assumed spherical particles at nodes in the positive and negative electrodes. The spherical particles are used to account for the effects of particle size, by solving the diffusion equation for the ion concentration across the cell:

$$\frac{\partial c_1}{\partial t} = D_s \left(\frac{\partial^2 c_1}{\partial r^2} + \frac{2}{r} \frac{\partial c_1}{\partial r} \right) \quad (21a)$$

with boundary conditions

$$\frac{\partial c_1}{\partial t} = 0 \text{ at } r = 0 \quad (21b)$$

$$\frac{i_{n,j}}{F} = -D_s \frac{\partial c_1}{\partial r} \text{ at } r = R_{s,j} \quad (21c)$$

where $j=n$ (anode) or p (cathode). In the liquid electrolyte:

$$\varepsilon \frac{\partial c_2}{\partial t} = \nabla \cdot (D_2^{eff} \nabla c_2) + \frac{1-t_+^0}{F} \nabla \cdot \mathbf{i}_2 - \frac{\mathbf{i}_2 \cdot \nabla t_+^0}{F} \quad (22)$$

In Eqns. (21) and (22), c_1 and c_2 denote the lithium-ion concentrations in the solid and liquid phases, respectively. A gradient of the chemical potential is the driving force for the lithium-ion diffusion across the width of the cell. In the existing model, the chemical kinetics at the particle-electrolyte interface is described using the Butler-Volmer equation, in which the flux on the particle surface is a function of the exchange current density and the surface overpotential, as shown in Eqn. (23):

$$i_{n,j} = i_{0,j} \left[\exp\left(\frac{\alpha_{\alpha,j} F}{RT} \eta_j\right) - \exp\left(-\frac{\alpha_{\alpha,j} F}{RT} \eta_j\right) \right] \quad (23)$$

In Eqn. (23) $\eta_j = \varphi_1 - \varphi_2 - U_{OCP}$ is the surface overpotential. The surface overpotential is estimated based on the electrical potentials in the solid (φ_1) and liquid (φ_2) phases, using Eqns. (24) and (25):

$$\nabla \cdot (\sigma \nabla \varphi_1) - J = 0 \quad (24)$$

$$\nabla \cdot (\kappa \nabla \varphi_2) + \nabla \cdot (\kappa_D \nabla (\ln c_2)) + J = 0 \quad (25)$$

The volumetric reaction current J is calculated using Eqn. (26), where $\varepsilon_{1,p}$ ($\varepsilon_{1,n}$) and $R_{s,p}$ ($R_{s,n}$) are the porosity and particle size in the positive (negative) electrode respectively. Further details of the porous electrode model can be found in refs. [38][39],[40].

$$J = \begin{cases} \left(\frac{3\varepsilon_1}{R_s}\right)_p i_{n,p} & \text{in the positive electrode} \\ 0 & \text{in the separator} \\ \left(\frac{3\varepsilon_1}{R_s}\right)_n i_{n,n} & \text{in the negative electrode} \end{cases} \quad (26)$$

Surrogate Modeling Process.

(a) Design of Experiments and Cross-Validation: The design variables considered in this study and their corresponding ranges are summarized in TABLE 6. DESIGN VARIABLES AND CORRESPONDING RANGES

. Since the focus of the study is on the cathode, the particle size and material properties apply to that electrode only. The

selected cycling rate range corresponds to typical automotive application requirements, while the particle sizes are consistent with those found in real electrodes [41]. The diffusion coefficient is known to be sensitive to the cell's state of charge, and reported values in the literature vary widely due to differences in electrode microstructure and measurement techniques [42]. Therefore, a wide diffusivity range needed to be considered to remain consistent with values reported in the literature. Further details of appropriate choices for the design ranges can be found in ref. [43]. A fixed thickness is assigned to all cell components: 100 μm for each electrode and 25 μm for the separator and each current collector. A uniform initial state of charge in each electrode is specified for each simulation, and the cell is discharged until the termination voltage of 2.0 V is reached.

TABLE 6. DESIGN VARIABLES AND CORRESPONDING RANGES

VARIABLE	SYMBOL	RANGE
Cycling rate	C	0.1~4 C
Particle radius	$R_{s,p}$	0.2~20 mm
Diffusivity	D_s	$0.1 \sim 10 \times 10^{-13} \text{ m}^2/\text{s}$
Conductivity	σ	1~100 S/m

Three types of surrogate models are considered in this study: polynomial response surface (PRS), kriging (KRG), and radial basis neural network (RBNN). For the kriging models, both first and second-order polynomial regressions are tested. In the RBNN models, the spread coefficient and error goal parameters are tuned to adjust the fit; however, the total number of neurons is fixed. For cross-validation of the PRS models, the adjusted coefficient of determination R_{adj}^2 is considered in addition to PRESS and independent test point prediction.

A preliminary design of experiments consisting of 25 points in a FCCD arrangement is initially selected to roughly evaluate the magnitude of effects of all design variables before constructing a comprehensive design of experiments. Since achieving a good surrogate model fit in a high-dimensional design space can be difficult [7], this first step is done to check for any variables that could be immediately removed from consideration, thus reducing the problem dimensionality. It is found that in all cases within the face-centered design, the effect of the electronic conductivity is negligible even when varied between its minimum and maximum values. This can also be verified with test points in the interior of the design space to check for interactions with other variables; in all cases varying the conductivity within the selected range causes less than a 1% change in the total cell energy. As a result, all subsequent analysis is performed on a reduced design space consisting of only the first three variables listed in TABLE 6. DESIGN VARIABLES AND CORRESPONDING RANGES

The initial design of experiments consisted of the 15 non-redundant points from the previous four design variable FCCD, in addition to 35 LHS points. However, error measures computed based on this initial design shows that it is too sparse to achieve sufficient model fit, with the minimum PRESS value being over 20% of the mean function value. Additionally, the region with high cycling rate, large particle size, and low diffusivity shows a sharp gradient in the specific energy, and the sparse distribution of points in this region contributes to poor overall model fit. To ensure a greater density of points in this sharp gradient region, a domain refinement is performed with an additional 100 design points in a logarithmic distribution.

Although this refinement improves model prediction in the previously sparse region, it also causes a shift in fidelity, leaving unacceptably large prediction errors elsewhere in the design space. To improve model fit in the entire design space, another refinement consisting of 165 design points selected using Latin hypercube sampling is made, resulting in a total of 315 points in the design of experiments. A kriging model constructed using this data set yields a PRESS value of 3.0% of the mean function value and a mean prediction error of 2.5% at 64 test points, suggesting a sufficient model fit to perform global sensitivity analysis.

(b) Glogal Sensitivity Analysis: Sensitivity indices computed from a wide range of surrogate models all indicate that the effects due to all three variables are strong, preventing further problem dimensionality reduction by direct variable elimination. However, it is also found that the global sensitivity indices vary among the different regions of the design space. As shown in Fig. 16, the effect of diffusivity vanishes in the diffusivity range above some critical value at about $1 \times 10^{-13} \text{ m}^2/\text{s}$. This diffusion-independence in the high-diffusivity range presents an opportunity to split the design space into multiple regions in which the problem dimensionality may be reduced for separate, more refined analysis.

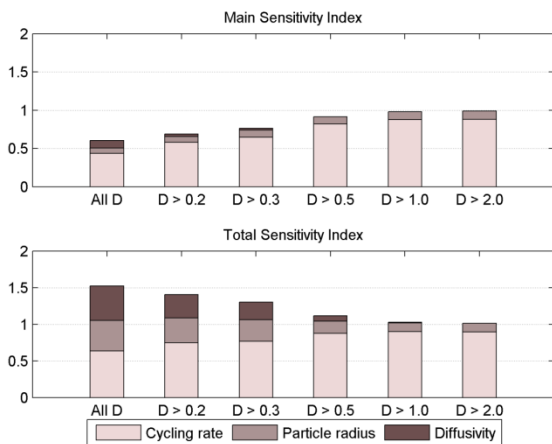


FIGURE 16. SENSITIVITY INDICES FOR KRG MODELS CONSTRUCTED ON SELECTED DIFFUSIVITY RANGES; UNITS ARE $10^{-13} \text{ m}^2/\text{s}$

(c) Dimensionality Reduction and Design Space Splitting: Within the low-diffusion range, it is found that the specific energy rapidly decreases with increasing discharge rate and particle size, as well as decreasing diffusivity. To further refine the analysis, we introduce a dimensionless time term τ to characterize the discharge and diffusion time scales:

$$\tau = \frac{D_s}{R_{s,p}^2 C} \quad (27)$$

As shown in Eqn. (27), this dimensionless time parameter combines all three design variables into a single expression relating the relative rates of the discharge and diffusion processes in the cell. As shown in Fig. 17, the specific energy decreases for low values of this parameter, where the diffusion rate is low compared to the required discharge rate. Also note the clear monotonic trend for values of $\tau < 0.2$. This suggests a further splitting of the diffusion-dependent region into a diffusion-limited region defined exclusively by the single dimensionless time parameter, and an intermediate region between the diffusion-limited and diffusion-independent regions, where all three variables are important. The process for splitting the design space and resulting sub-regions are summarized in Fig. 18.

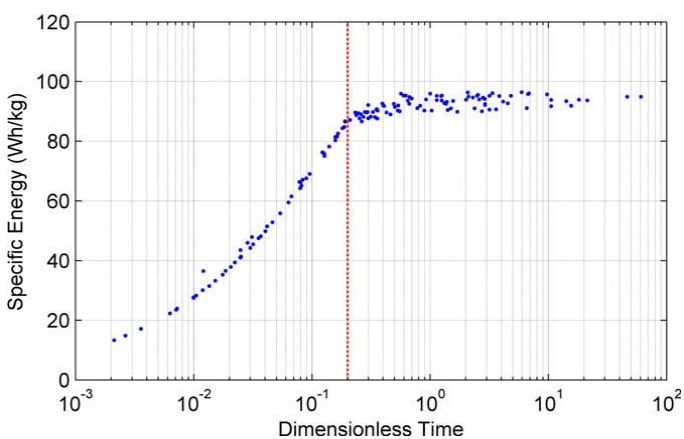


FIGURE 17. SPECIFIC ENERGY VS. DIMENSIONLESS TIME, FOR $D_s < 1 \times 10^{-13} \text{ m}^2/\text{s}$

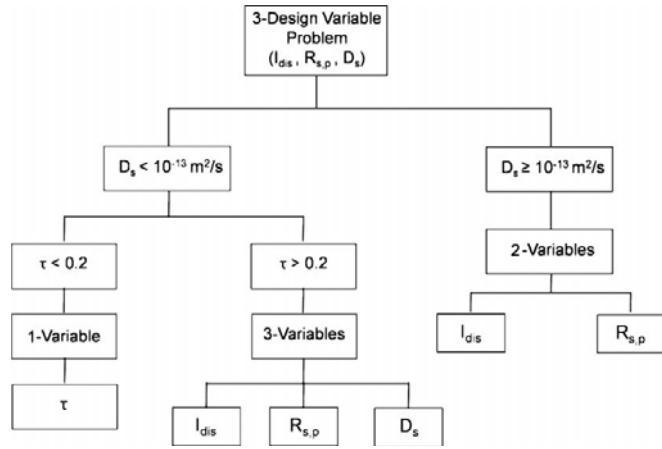


FIGURE 18. PROCESS FOR SPLITTING DESIGN SPACE INTO SEPARATE REDUCED-DIMENSIONALITY REGIONS BASED ON SENSITIVITY INDICES AND CRITICAL DIFFUSION VALUES

To assess the effect of design space splitting on surrogate model fit, various error measures are computed for the best of each surrogate model type and compared between the non-split model for the entire design space and the split sub-regions. The results are summarized in Tab. 7, which shows significantly improved model fit in each split sub-region when compared to the single model for the entire domain. Perhaps more importantly, this improved model fit can be achieved without requiring any new data. Line and surface plots for the specific energy in the split sub-regions are shown in Fig. 19; the energy decreases rapidly at very low values of the dimensionless time parameter, as well as high cycling rates and large particle sizes. A weaker diffusivity effect can be observed in Fig. 19(b); however, the diffusivity effects are strongest in the diffusion-limited region where they are reflected in the dimensionless time parameter.

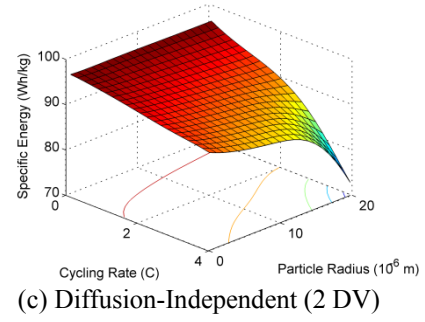
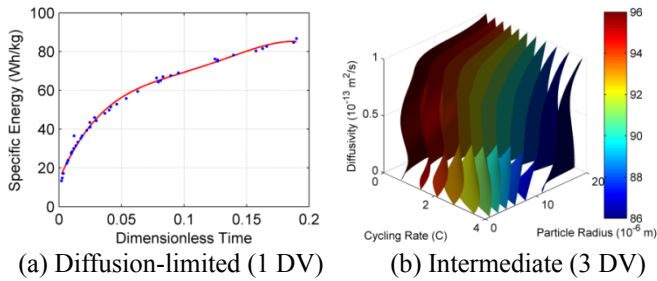


FIGURE 19. SPECIFIC ENERGY AS A FUNCTION OF THE DESIGN VARIABLES

(d) Multiobjective Optimization: The preceding results have shown that specific energy can be increased by reducing the discharge rate. However, the discharge rate is also directly related to the battery cell's power output, another critical objective. Since the power is directly dependent on the discharge current, a competing effect can be expected between specific energy, which favors low cycling rates, and specific power, which favors higher rates. To quantify these competing effects, a Pareto front is constructed from additional randomly sampled points and fitted with the split surrogate models shown in Tab. 7.

TABLE 7. EFFECT OF DESIGN SPACE SPLITTING ON PERFORMANCE METRICS

Surrogate	Parameter	Non-split	Split		
			Diffusion-limited	Intermediate	Diffusion-independent
	Design points	315	42	32	236
	Design variables	3	1	3	2
PRS	R_{adj}^2	0.875	0.995	0.997	0.932
	RMSE (%)	6.98	3.99	0.09	0.87
	PRESS (%)	8.11	6.29	0.84	0.95
	RMS test error (%)	10.0	-	0.48	-
	Max test error (%)	34.6	-	1.46	-
KRG	PRESS (%)	3.50	5.21	0.43	1.53
	RMS test error (%)	5.24	-	0.65	-
	Max test error (%)	21.2	-	1.96	-
RBNN	PRESS (%)	6.05	-	1.39	4.63
	RMS test error (%)	7.34	-	1.06	-
	Max test error (%)	29.2	-	2.79	-

	error (%)				
--	-----------	--	--	--	--

Specific power data are fit by constructing an additional 4th order PRS model. The resulting Pareto front is shown in Fig. 20.

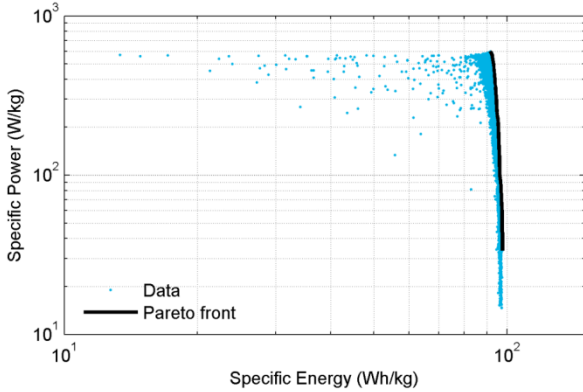


FIGURE 20. PARETO FRONT SHOWING TRADEOFF BETWEEN SPECIFIC ENERGY AND SPECIFIC POWER.

The front shows stiffness in favor of high power, which can be achieved with relatively little sacrifice in energy. However, a greater amount of scatter in the specific energy data can also be observed as the specific power is increased. This suggests that the cell performance becomes increasingly sensitive to the other design variables as the cycling rate is increased, resulting in a greater penalty for large particle size or low diffusivity in the cathode.

Major Outcome. For simplicity, it is often preferable to represent a full design space with a single surrogate model. However, due to the difficulty encountered in attempting to achieve a reasonable model fit with a single global surrogate, a split design space strategy is adopted instead. Although the splitting of the design space does not provide any advantage in terms of computational speed, it does allow for much improved surrogate model fit as shown in Tab. 7, even in the intermediate region in which a reduction in dimensionality did not occur. This is likely due to differing dominant physical phenomena within the design space, as suggested by the shift in fidelity caused by the initial domain refinement and the dimensionless time scale analysis. The improved surrogate model performance is critically important to the construction of a meaningful Pareto front to study the competition between specific energy and specific power.

SUMMARY AND CONCLUSIONS

In this paper, we present three case studies that fall under different domains of engineering, namely cavitation, dielectric barrier discharge (DBD), and lithium-ion batteries. The cost and time constraints associated with each of the problems are

highlighted. To enable the design of better engineered systems, different criteria may be applied. Validated cavitation model parameters are needed that can predict its onset. On the other hand, operating and material conditions that achieve better performance goals are not known for DBD. In lithium-ion batteries, the effect of simultaneous variation of several design variables on its performance should be quantified.

Surrogate modeling and analysis offers a unique design tool for each of these problems:

- (i) The surrogate analysis is used to assess
 - (a) the sensitivity of the cavitation model to parameters and uncertainties in the thermal-sensible material properties,
 - (b) impact of waveform, frequency and dielectric constant on DBD performance, and
 - (c) the relative importance of discharge rate, particle size, diffusivity and conductivity of battery performance.
- (ii) The surrogate models can be particularly useful in analyzing competing objectives, such as the accuracy of temperature and pressure prediction in cavitation, power input and force generation in DBD, and specific energy and power in lithium-ion batteries.
- (iii) The surrogate-based global sensitivity analysis facilitates identification of dominating and less-influential design variables. Based on the insight gained, dimensionality reduction can be conducted to reduce the complexity of the issues. This benefit is particularly significant for complex problems which are expensive to simulate/test and involve a large number of design variables. For instance, it is shown that
 - (a) the condensation term has minimal influence on the cavitation model compared to the evaporation term,
 - (b) the dielectric constant is always influential, but the importance of frequency and time ratio alternates depending on low and high power capability, and
 - (c) the dimensionality of the battery case can be reduced based on the diffusivity of the solid, which could be ignored from the analysis beyond a certain critical value.
- (iv) In addition to sensitivity analysis, surrogate tools offer the capability to identify optimal solutions in regions where competing objectives may be present. In such cases, construction of a Pareto front can assist in elucidating the gain achieved by sacrificing the other objectives. In the context of the case studies presented, we show that multiple Pareto fronts, which may be disconnected with each other, may also exist, as evident in the case of DBD. For cavitation, it was shown that a selected value of the evaporation model parameter minimizes the pressure difference through a small penalty in the temperature difference. Since pressure prediction is more critical in design of components that may be subjected to heavy loads, the tradeoff between pressure and temperature is beneficial in this situation. In the case of lithium-ion batteries, the high slope of the Pareto front suggests that substantial gain in power, which is desirable for power-

tools and automotive applications, can be achieved through minor sacrifice in energy storage.

In summary, we have developed a surrogate-based framework to assess the role of design variables on multiple competing objectives for a wide range of engineering problems. The framework allows for both local and global domain refinement strategies to be utilized in conjunction with multiple error criteria to estimate and reduce uncertainties, since a single criterion may lead to high errors. These techniques prove to be very valuable in advancing the capabilities of surrogate modeling. Similar approaches can be extended to numerous other thermo-fluid and energy systems.

REFERENCES

- [1] Papila, N., Shyy, W., Griffin, L., and Dorney, D.J., 2002, "Shape Optimization of Supersonic Turbines Using Global Approximation Methods", *J. Prop. Power*, **18**, pp. 509-518.
- [2] Shyy, W., Papila, N., Vaidyanathan, R., and Tucker, P.K., 2001, "Global Design Optimization for Aerodynamics and Rocket Propulsion Components", *Prog. Aero. Sci.*, **37**, pp. 59-118.
- [3] McKay, M.D., Beckman, R.J., and Conover, W.J., 1979, "A Comparison of Three Methods of Selecting Values of Input Variables in the Analysis of Output from a Computer Code", *Technometrics*, **21**, pp. 239-245.
- [4] Myers, R.H., and Montgomery, D.C., 1995, *Response Surface Methodology: Process and Product in Optimization Using Designed Experiments*, 1st ed., Wiley and Sons Inc.
- [5] Queipo, N.V., Haftka, R.T., Shyy, W., Goel, T., Vaidyanathan, R., and Tucker, P.K., 2005, "Surrogate-based analysis and optimization", *Prog. Aero. Sci.*, **41**, pp. 1-28.
- [6] Lophaven, S.N., Nielsen, H.B., and Sondergaard, J., 2002, DACE – A Matlab kriging toolbox. Version 2.0, Technical Report, IMM-TR-2002-12, Technical University of Denmark, Denmark.
- [7] Goel, T., Dorney, D.J., Haftka, R.T., and Shyy, W., 2008, "Improving the hydrodynamic performance of diffuser vanes via shape optimization", *Comp. Fluids*, **37**, pp. 705-723.
- [8] Goel, T., Haftka, R.T., Shyy, W., and Queipo, N.V., 2007, "Ensemble of surrogates", *Struct. Multidisc. Optim.*, **33**, pp. 199-216.
- [9] Goel, T., Haftka, R.T., and Shyy, W., 2009, "Comparing error estimation measures for polynomial and kriging approximation of noise-free functions", *Struct. Multidisc. Optim.*, **38**, pp. 429-442.
- [10] Sobol, I., 1993, "Sensitivity estimates for non-linear mathematical models", *Math. Modeling Comput. Exp.*, **4**, pp. 407-414.
- [11] Mack, Y., Goel, T., Shyy, W., and Haftka, R., 2007, "Surrogate model-based optimization framework: a case study in aerospace design", *Stud. Comp. Intel.*, **51**, pp. 323-342.
- [12] Utturkar, Y., Wu, J., Wang, G., and Shyy, W., 2005, "Recent Progress in Modeling of Cryogenic Cavitation for Liquid Rocket Propulsion", *Prog. Aero. Sci.*, **41**, pp. 558-608.
- [13] Knapp, R.T., Daily, J.W., and Hammit, F.G., 1970, *Cavitation*, McGraw-Hill, New York.
- [14] Brennen, C.E., 1995, *Cavitation and bubble dynamics*, Oxford Engineering & Sciences Series, Oxford University Press, New York.
- [15] Joseph, D.D., 1995, "Cavitation in a flowing liquid", *Phys. Rev. E*, **51**(3), pp. 1649-1650.
- [16] Joseph, D.D., 1998, "Cavitation and the state of stress in a flowing liquid", *J. Fluid Mech.*, **366**, pp. 367-378.
- [17] Lemmon, E.W., McLinden, M.O., and Huber, M.L., 2002, REFPROP: Reference Fluid thermodynamic and transport properties. NIST Standard Database 23, version 7.0.
- [18] Goel, T., Thakur, S., Haftka, R.T., Shyy, W., and Zhao, J., 2008, "Surrogate Model-Based Strategy for Cryogenic Cavitation Model Validation and Sensitivity Evaluation", *Int. J. Numer. Meth. Fluids*, **58**, pp. 969-1007.
- [19] Tseng, C., and Shyy, W., 2009, "Surrogate-based modeling of cryogenic turbulent cavitating flows", In Proceedings of the 7th International Symposium on Cavitation, CAV2009, Paper No. 77, Ann Arbor, Michigan, USA.
- [20] Tseng, C., and Shyy, W., 2010, "Modeling for isothermal and cryogenic cavitation", *Int. J. Heat Mass Transfer*, **53**, pp. 513-525.
- [21] Wang, G., Senocak, I., Shyy, W., Ikohagi, T., and Cao, S., 2001, "Dynamics of attached turbulent cavitating flows", *Prog. Aero. Sci.*, **37**, pp. 551-581.
- [22] Senocak, I., and Shyy, W., 2004, "Interfacial dynamics-based modeling of turbulent cavitating flows, part-1: model development and steady-state computations", *Int. J. Numer. Meth. Fluids*, **44**, pp. 975-995.
- [23] Venkateswaran, S., Lindau, J.W., Kunz, R.F., and C.L. Merkle, 2002, "Preconditioning Algorithms for the Computation of Multiphase Mixture Flows", *J. Comp. Phys.*, **179**, pp. 1-29.
- [24] Hord, J., 1973, "Cavitation in liquid cryogenics II-hydrofoil", NASA CR-2156.
- [25] McDaniel, E.W., 1964, *Collision phenomena in ionized gases*, John Wiley & Sons, New York.
- [26] Mitchner, M., and Kruger Jr., C.H., 1973, *Partially ionized gases*, John Wiley & Sons, New York.
- [27] Roth, J.R., and Sherman, D.M., 1998, "Boundary layer flow control with a one atmosphere uniform glow discharge surface plasma", 36th AIAA Aerospace Sciences Meeting and Exhibit, AIAA Paper 98-0328, Reno, NV.
- [28] Shyy, W., Jayaraman, B., and Andersson, A., 2002, "Modeling of glow discharge-induced fluid dynamics", *J. Appl. Phys.*, **92**(11), pp. 6434-6443.
- [29] Porter, C.O., Baughn, J.W., McLaughlin, T.E., Enloe, C.L., and Font, G.I., 2007, "Plasma actuator force measurements", *AIAA J.*, **45**(7), pp. 1562-1570.

- [30] Jukes, T.N., Choi, K., Johnson, G.A., and Scott, S.J., 2006, "Characterization of surface plasma-induced wall flows through velocity and temperature measurements", *AIAA J.*, **44**(4), pp. 764-771.
- [31] Forte, M., Jolibois, J., Moreau, E., Touchard, G., Cazalens, M., 2006, "Optimization of a dielectric barrier discharge actuator by stationary and non-stationary measurements of the induced flow velocity - application to airflow control", 3rd AIAA Flow Control Conference, AIAA Paper 2006-2863, San Francisco, CA.
- [32] Abe, T., Takizawa, Y., Sato, S., and Kimura, N., 2007, "A parametric experimental study for momentum transfer by plasma actuator", 45th Aerospace Sciences Meeting and Exhibit, AIAA Paper 2007-187, Reno, NV.
- [33] Roth, J.R., and Dai, X., 2006, "Optimization of the aerodynamic plasma actuator as an electrohydrodynamic (EHD) electrical device", 44th AIAA Aerospace Sciences Meeting and Exhibit, AIAA Paper 2006-1203, Reno, NV.
- [34] Jayaraman, B., Tharkur, S., and Shyy, W., 2007, "Modeling of fluid dynamics and heat transfer induced by dielectric barrier plasma actuator", *J. Heat Trans.*, **129**, pp. 517-525.
- [35] Jayaraman, B., and Shyy, W., 2008, "Modeling of dielectric barrier discharge-induced fluid dynamics and heat transfer", *Prog. Aero. Sci.*, **44**, pp. 139-191.
- [36] Ward, A.L., 1962, "Calculations of cathode-fall characteristics", *J. Appl. Phys.*, **33**(9), pp. 2789-2974.
- [37] Jayaraman, B., Cho, Y., and Shyy, W., 2008, "Modeling of dielectric barrier discharge plasma actuator", *J. Appl. Phys.*, **103**, pp. 053304.
- [38] Doyle, M., Fuller, T.F., and Newman, J., 1993, "Modeling of galvanostatic charge and discharge of the lithium/polymer/insertion cell", *J. Electrochem. Soc.*, **140**, pp. 1526-1533.
- [39] Fuller, T.F., Doyle, M., and Newman, J., 1994, "Simulation and optimization of the dual lithium ion insertion cell", *J. Electrochem. Soc.*, **141**, pp. 1-10.
- [40] Doyle, M., Newman, J., Gozdz, A.S., Schmutz, C.N., and Tarascon, J.-M., 1996, "Comparison of modeling predictions with experimental data from plastic lithium ion cells", *J. Electrochem. Soc.*, **143**, pp. 1890-1903.
- [41] Lu, C.-H., and Lin, S.-W., 2001, "Influence of the particle size on the electrochemical properties of lithium manganese oxide", *J. Power Sources*, **97-98**, pp. 458-460.
- [42] Zhang, D., Popov, B.N., and White, R.E., 2000, "Modeling lithium intercalation of a single spinel particle under potentiodynamic control", *J. Electrochem. Soc.*, **147**, pp. 831-838.
- [43] Du, W., Gupta, A., Zhang, X., Sastry, A.M., and Shyy, W., 2010, "Effect of cycling rate, particle size and transport properties on lithium-ion cathode performance", *Int. J. Heat Mass Trans.*, **53**, pp. 3552-3561.